

# Updated High-Temperature Opacities for The Dartmouth Stellar Evolution Program and their Effect on the Jao Gap Location

THOMAS M. BOUDREAU<sup>1</sup> AND BRIAN C. CHABOYER<sup>1</sup>

<sup>1</sup>*Department of Physics and Astronomy, Dartmouth College, Hanover, NH 03755, USA*

## ABSTRACT

The Jao Gap, a 17 percent decrease in stellar density at  $M_G \sim 10$  identified in both Gaia DR2 and EDR3 data, presents a new method to probe the interior structure of stars near the fully convective transition mass. The Gap is believed to originate from convective kissing instability wherein asymmetric production of  $\text{He}^3$  causes the core convective zone of a star to periodically expand and contract and consequently the stars' luminosity to vary. Modeling of the Gap has revealed a sensitivity in its magnitude to a population's metallicity primarily through opacity. Thus far, models of the Jao Gap have relied on OPAL high-temperature radiative opacities. Here we present updated synthetic population models tracing the Gap location modeled with the Dartmouth stellar evolution code using the OPLIB high-temperature radiative opacities. Use of these updated opacities changes the predicted location of the Jao Gap by  $\sim 0.05$  mag as compared to models which use the OPAL opacities.

*Keywords:* Stellar Evolution (1599) — Stellar Evolutionary Models (2046)

## 1. INTRODUCTION

Due to initial mass requirements of the molecular clouds which collapse to form stars, star formation is strongly biased towards lower mass, later spectral class, stars when compared to higher mass stars. Partly as a result of this bias and partly as a result of their extremely long main-sequence lifetimes, M-dwarfs make up approximately 70 percent of all stars in the galaxy. Moreover, some planet search campaigns have focused on M-dwarfs due to the relative ease of detecting small planets in their habitable zones (e.g. [Nutzman & Charbonneau 2008](#)). M-dwarfs then represent both a key component of the galactic stellar population as well as the possible set of stars which may host habitable exoplanets. Given this key location M-dwarfs occupy in modern astronomy it is important to have a thorough understanding of their structure and evolution.

[Jao et al. \(2018\)](#) discovered a novel feature in the Gaia DR2  $G_{BP} - G_{RP}$  color-magnitude-diagram. Around  $M_G = 10$  there is an approximately 17% decrease in stellar density of the sample of stars [Jao et al.](#) consid-

ered. Subsequently, this has become known as either the Jao Gap, or Gaia M dwarf Gap. Following the initial detection of the Gap in DR2 the gap has also potentially been discovered in 2MASS ([Jao et al. 2018](#)); however, this the Significance of this detection is weak and it relies on the prior of the gaps location from Gaia data. Further, both EDR3 data and DR3 data also reveal the gap ([Jao & Feiden 2020](#)) [[Check on these citations and find a citation for DR3](#)]. These three data sets sources provided a clear picture that this feature is real and not an bias inherent to DR2.

This gap is generally attributed to convective instabilities in the cores of stars straddling the fully convective transition mass ( $0.3 - 0.35 M_\odot$ ) ([Baraffe & Chabrier 2018](#)). These instabilities interrupt the normal, slow, main sequence luminosity evolution of a star and resulting in lower than expected luminosities [[WORDING](#)] ([Jao & Feiden 2020](#)).

The Jao Gap, inherently a feature of M dwarf populations, provides an enticing and unique view into the interior physics of these stars ([Feiden et al. 2021](#)). This is especially important as, unlike more massive stars, M dwarf seismology is currently infeasible due to the short periods and extremely small magnitude's which both radial and low-order low-degree non-radial seismic waves are predicted to have in such low mass stars ([Rodríguez-López 2019](#)). The Jao Gap therefore provides one of the

only current methods to probe the interior physics of M dwarfs (e.g Feiden et al. 2021; Mansfield & Kroupa 2021, [ARE THESE THE BEST PAPERS TO CITE HERE?]).

Despite the early success modeling the Gap some issues remain. Jao & Feiden identify that the gap has a wedge shape which has not been successful reproduced by any current modeling efforts and which implies a somewhat unusual population composition of young, metal-poor stars. Further, Feiden et al. (2021) identify substructure, an additional over density of stars, directly below the Gap, again a feature not yet fully captured by current models.

All currently published [pretty sure this is correct but DOUBLE CHECK THAT IT IS ALL OF THEM] models of the Jao Gap make use of OPAL high temperature radiative opacities. Here we investigate the affect of using the more up to date OPLIB high temperature radiative opacities and whether these opacity tables bring models more in line with observations. In section 2 we provide an overview of the physics believed to result in the Jao Gap, in section ?? we review the differences between OPAL and OPLIB and describe how we update DSEP to use OPLIB opacity tables. In section ?? we validate the update opacities by generating solar calibrated stellar models. Section 5 walks through the stellar evolution and population synthesis modelling we preform and finally section 6 presents our findings. [Make this more active]

## 2. JAO GAP

A theoretical explanation for the Jao Gap (Figure 1) comes from van Saders & Pinsonneault (2012), who propose that in a star directly above the transition mass, due to asymmetric production and destruction of  $\text{He}^3$  during the proton-proton I chain (ppI), periodic luminosity variations can be induced. This process is known as convective-kissing instability. Such a star will descend the pre-main sequence with a radiative core; however, as the star reaches the zero age main sequence (ZAMS) and as the core temperature exceeds  $7 \times 10^6$  K, enough energy will be produced by the ppI chain that the core becomes convective. At this point the star exists with both a convective core and envelope, in addition to a thin, radiative, layer separating the two. Subsequently, asymmetries in ppI affect the evolution of the star’s convective core.

The proton-proton I chain constitutes three reactions

1.  $p + p \longrightarrow d + e^+ + \nu_e$
2.  $p + d \longrightarrow {}^3\text{He} + \gamma$
3.  ${}^3\text{He} + {}^3\text{He} \longrightarrow {}^3\text{He} + 2p$

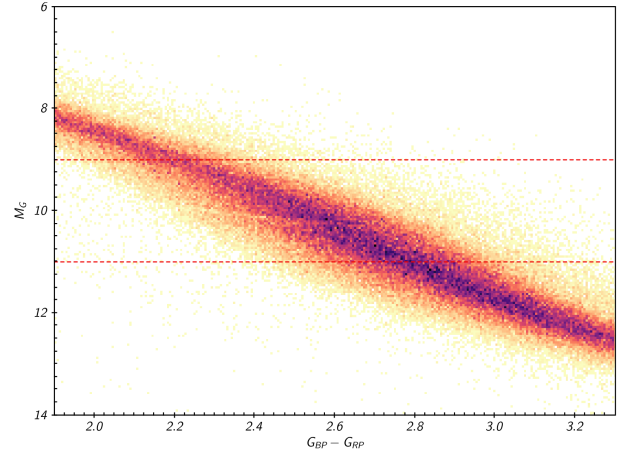


**Figure 1.** Figure 1 from Jao et al. (2018) showing the so called “Jao Gap” at  $M_G \approx 10$  [SHOULD I REMAKE THIS USING DR3 DATA?]

Because reaction 3 of ppI consumes  ${}^3\text{He}$  at a slower rate than it is produced by reaction 2, core  ${}^3\text{He}$  abundance, and consequently the rate of reaction 3, increases with time. The core convective zone expands as more of the star becomes unstable to convection. This expansion continues until the core connects with the convective envelope. At this point convective mixing can transport material throughout the entire of the star and the high concentration of  ${}^3\text{He}$  rapidly diffuses outward, away from the core, decreasing energy generation as reaction 3 slows down. Ultimately, this leads to the convective region around the core pulling back away from the convective envelope, leaving in place the radiative transition zone, at which point  ${}^3\text{He}$  concentrations grow in the core until it once again expands to meet the envelope. These periodic mixing events will continue until the  ${}^3\text{He}$  concentration throughout the star reach an equilibrium ultimately resulting in a fully convective star. Figure 2 traces the evolution of a characteristic star within the Jao Gap’s mass range.

### 2.1. Modeling the Gap

Since the identification of the Gaia M-dwarf gap, stellar modeling has been conducted to better constrain its location, effects, and exact cause. Both Mansfield & Kroupa (2021) and Feiden et al. (2021) identify that the gap’s mass location is correlated with model metallicity — the mass-luminosity discontinuity in lower metallicity models being at a commensurately lower mass. Feiden et al. (2021) suggests this dependence is due to the steep relation of the radiative temperature gradient,  $\nabla_{rad}$ , on temperature and in turn, on stellar mass.

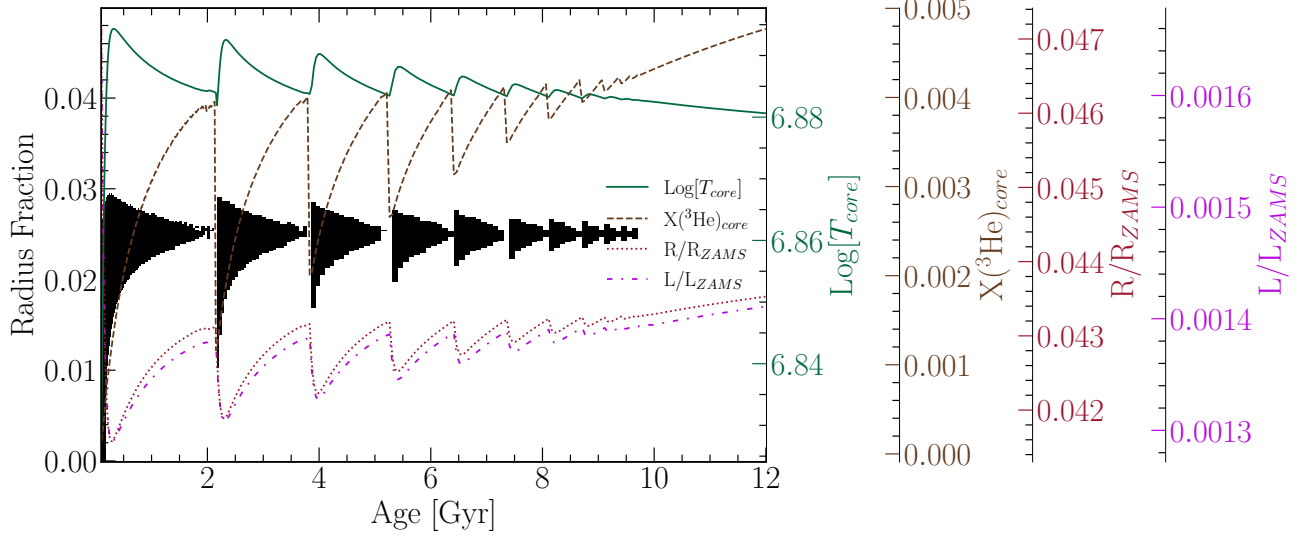


**Figure 2.** Kippenhan diagram for a charectaristic stellar model of  $0.35625 M_{\odot}$  which is within the Jao Gap’s mass range. The black shaded regions denote whether, at a particular model age, a radial shell within the model is radiative or convective (with white meaning convective and black meaning radiative). The lines trace the models cote temperature, core  $^3\text{He}$  mass fraction, fractional luminosity wrt the zero age main sequence and fractional radius wrt. the zero age main sequence.

$$\nabla_{\text{rad}} \propto \frac{L\kappa}{T^4} \quad (1)$$

As metallicity decreases so does opacity, which, by Equation 1, dramatically lowers the temperature where radiation will dominate energy transport (Chabrier & Baraffe 1997). Since main sequence stars are virialized the core temperature is proportional to the core density and total mass (Equation 2). Therefore, if the core temperature where convective-kissing instability is expected decreases with metallicity, so too will the mass of stars which experience such instabilities.

$$T_c \propto \rho_c M^2 \quad (2)$$

This strong opacity dependence presents a slight problem where modeling is concerned. With current computational tools it is infeasible to compute opacities on the fly; rather, Rossland Mean opacity ( $\kappa_R$ ) for individual elements must be pre-tabulated over a wide range of temperatures and densities. These opacities can then be somewhat arbitrarily mixed together and interpolated to form opacity lookup-tables. Multiple groups have performed these calculations and subsequently made tables available to the wider community, these include the Opacity Project (OP Seaton et al. 1994), Laurence Livermore National Labs OPAL opacity tables (Iglesias & Rogers 1996), and Los Alamos National Labs OPLIB opacity tables (Colgan et al. 2016).

### 3. UPDATED OPACITIES

OPAL high-temperature radiative opacity tables in particular are very widely used by current generation isochrone grids (e.g. Dartmouth, MIST, & StarEvol, Dotter et al. 2008; Choi et al. 2016; Amard et al. 2019). However, there are two primary issues with these tables, one, they are relatively old and therefore do not incorporate the most up to date understanding of plasma modeling in their code [CITATION], and two, they report rossland mean opacities to only **N** digits [WHICH IS AN ISSUE WHY?].

While the two issues given above should have relatively small affects, the strong theoretical opacity dependence of the Jao Gap raises the potential for these small effects to measurably shift the gap’s location. In order to address both the out of date plasma modeling and the low numeric presicion we update DSEP to use high temperature opacity tables based on measurements from Los Alamos national Labs T-1 group (OPLIB, Colgan et al. 2016). The OPLIB tables use the much more up-to-date ATOMIC plasma modeling code [CITATION] in addition to reporting rossland mean opacities to **N** digits of numeric presicion.

ATOMIC (Magee et al. 2004) is a LTE and non-LTE opacity and plasma modeling code. A major strength of ATOMIC when compared to the older plasma modeling programs is its ability to vary its refinement level (Fontes et al. 2015). [OTHER DIFFERENCES] For a more detailed breakdown of how the most up-to-date set of OPLIB tables are generated see (Colgan et al. 2016).

The most up to date OPLIB tables include monochromatic Rosseland mean opacities — composed from

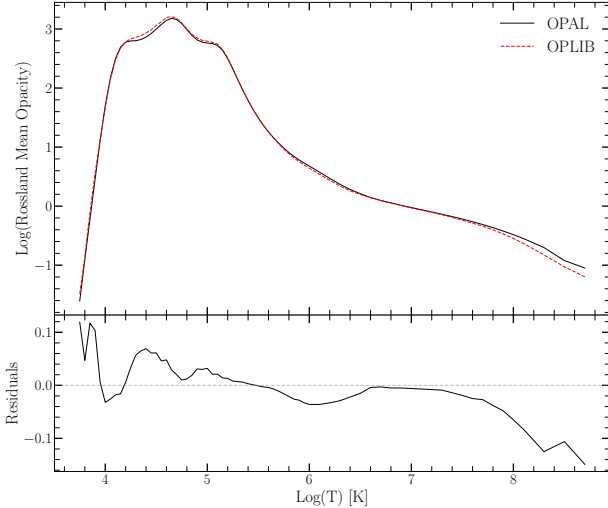


**Figure 3.** Rosseland mean opacity with the GS98 solar composition for both OPAL opacities and OPLIB opacities (top). Residuals between OPLIB opacities and OPAL opacities (bottom). These opacities are plotted at  $\log_{10}(R) = -1.5$ ,  $X = 0.7$ , and  $Z = 0.02$ . Note how the OPLIB opacities are systematically lower than the OPAL opacities for temperatures above  $10^6$  K.

bound-bound, bound-free, free-free, and scattering opacities — for elements hydrogen through zinc over temperatures 0.5eV to 100 keV and for mass densities from approximately  $10^{-8}$  g cm $^{-3}$  up to approximately  $10^4$  g cm $^{-3}$  (though the exact mass density range varies as a function of temperature).

When comparing OPAL and OPLIB opacity tables (Figure 3) we find OPLIB opacities are systematically lower than OPAL opacities for temperature above  $10^6$  K (Figure 3). These lower opacities will result the temperature where radiation dominates energy transport lowering [CITATION?]. Consequently, the radiative layer in stellar models evolved using OPLIB opacity tables will be [further?] out from the models center than it would be in models making use of OPAL tables.

### 3.1. Table Querying and Conversion

DSEP, along with most other stellar evolution programs, uses pre-computed high-temperature opacity tables. Specifically, these tables list the Rosseland-mean opacity,  $\kappa_R$ , along three dimensions: temperature, a density proxy  $R$ , and composition.  $R$  is defined as

$$R = \frac{\rho}{T_6^3} \quad (3)$$

Where  $T_6 = T \times 10^{-6}$  and  $\rho$  is the mass density. If  $T$  and  $\rho$  are given in cgs then for much of the radius of a star  $\log(R) \sim -1.5$  [CITATION].  $R$  is used, as opposed to simply tracking opacity over mass density, because of

its small dynamic range when compared to  $\rho$  ( $\rho \sim 10^5$  [g cm $^{-3}$ ] at the core of an RGB star all the way down to  $\sim 10^{-8}$  [g cm $^{-3}$ ] within the envelope).

OPLIB tables are queried from a web interface<sup>1</sup>. In order to generate many tables easily and quickly we develop a web scraper built with Python’s `requests` module in addition to the 3rd party `mechanize` and `BeautifulSoup` modules (Chandra & Varanasi 2015; Richardson 2007) which can get tables with minimal intervention. This web scraper submits a user requested chemical composition (composed of mass fractions for elements from Hydrogen to Zinc) to the Los Alamos web form, selects 0.0005 keV as the lower temperature bound and 60 keV as the upper temperature bound, and finally requests opacity measurements for 100 densities, ranging from  $1.77827941 \times 10^{-15}$  [g cm $^{-3}$ ] up to  $1 \times 10^7$  [g cm $^{-3}$ ], at each temperature interval. These correspond to approximately the same temperature and density range of opacities present in the OPAL opacity tables.

OPLIB reports  $\kappa_R$  as a function of mass density, temperature in keV, and composition. Recall that DSEP accepts tables where opacity is given as a function of temperature in Kelvin,  $R$ , and composition. The conversion from temperature in keV to Kelvin is trivial

$$T_K = T_{keV} * 11604525.0061657 \quad (4)$$

However, the conversion from mass density to  $R$  is more involved. Because  $R$  is coupled with both mass density and temperature there is no way to directly convert tabulated values of opacity reported in the OPLIB tables to their equivalents in  $R$  space. Instead we must rotate the tables, interpolating  $\kappa_R(\rho, T_{eff}) \rightarrow \kappa_R(R, T_{eff})$ .

To preform this rotation we use the `interp2d` function within `scipy`’s `interpolate` (Virtanen et al. 2020) module to construct a cubic bivariate B-spline (DIERCKX 1981) interpolating function  $s$ , with a smoothing factor of 0, representing the surface  $\kappa_R(\rho, T_{eff})$ . For each  $R^i$  and  $T_{eff}^j$  which DSEP expects high-temperature opacities to be reported for, we evaluate Equation 3 to find  $\rho^{ij} = \rho(T_{eff}^j, R^i)$ . Opacities in  $T_{eff}$ ,  $R$  space are then inferred as  $\kappa_R^{ij}(R^i, T_{eff}^j) = s(\rho^{ij}, T_{eff}^j)$ .

As first-order validation of this interpolation scheme we can preform a similar interpolation in the opposite direction, rotating the tables back to  $\kappa_R(\rho, T_{eff})$  and then comparing the initial, “raw”, opacities to those which have gone through the interpolations process. Figure 4 shows the fractional difference between the raw opac-

<sup>1</sup> <https://aphysics2.lanl.gov/apps/>



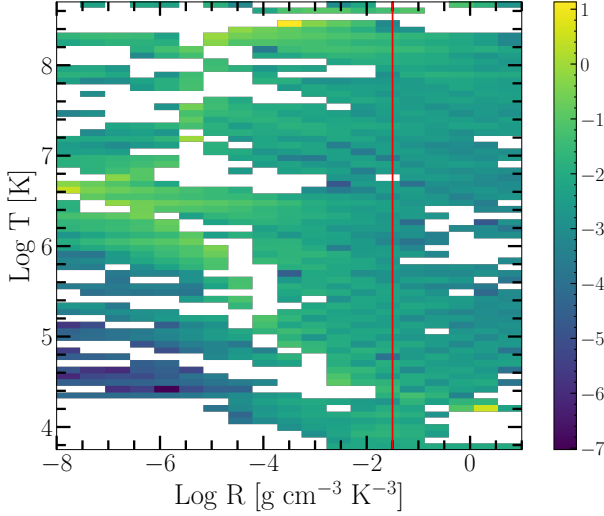


**Figure 4.** Log Fractional Difference between opacities in  $\kappa_R(\rho, T_{eff})$  space directly queried from the OPLIB webform and those which have been interpolated into  $Log(R)$  space and back. Note that, due to the temperature grid DSEP uses not aligning perfectly which the temperature grid OPLIB uses there may be edge effects where the interpolation is poorly constrained. The red line corresponds to  $Log(R) = -1.5$  where much of a stellar model's radius exists.

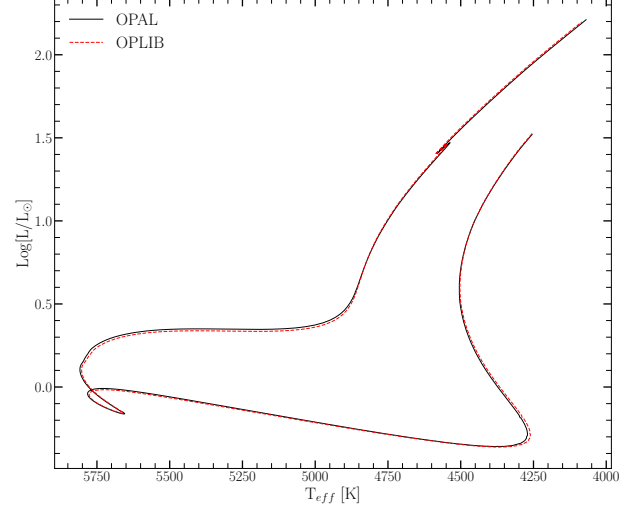


**Figure 5.** HR Diagram for the two SCSMs, OPAL and OPLIB. OPLIB is show as a grey dashed line.

Model	$X$	$\alpha_{ML}$
OPAL	0.7066	1.9333
OPLIB	0.7107	1.9629

**Table 1.** Optimized parameters for SCSMs evolved using OPAL and OPLIB high temperature opacity tables.

ities and a set which have gone through this double  
interpolation. The red line denotes  $Log(R) = -1.5$   
where models will tend to sit for much of their radi-  
us. Along the  $Log(R) = -1.5$  line the mean frac-  
tional difference is  $\langle \delta \rangle = 0.006$  with an uncertainty of  
 $\sigma_{\langle \delta \rangle} = 0.009$ . One point of note is that, because the  
initial rotation into  $Log(R)$  space also reduces the do-  
main of the opacity function interpolation-edge effects  
which we avoid initially by extending the domain past  
what DSEP needs cannot be avoided when interpolating  
back into  $\rho$  space. **[IS THERE SOME MORE CLEAR  
VALIDATION WHICH I SHOULD PREFORM?]**

#### 4. SOLAR CALIBRATED STELLAR MODELS

In order to validate the OPLIB opacities, we generate  
a solar calibrated stellar model (SCSM) using these new  
tables. We allow both the convective mixing length pa-  
rameter,  $\alpha_{ML}$ , and the initial Hydrogen mass fraction,  
 $X$ , to vary simultaneously, minimizing the difference  
between resultant models' final radius and luminosity  
to those of the sun.

Optimization of  $\alpha_{ML}$  and  $X$  is conducted using gradi-  
ent descent. For each optimization step three models are  
evolved: a reference model, a model with a small per-  
turbation to the hydrogen mass fraction but the same  
mixing length as the reference model, and a model with  
a small perturbation to the mixing length but the same  
hydrogen mass fraction as the reference. Perturbations

are sampled from a normal distribution (implemented  
though `numpy.random`). This distribution is sampled  
and that sample is then added to the reference value  
for either  $X$  or  $\alpha_{ML}$ . The luminosity and radius of the  
three evolved models are compared to solar values and  
the gradient of the resultant  $L - L_{\odot}$ ,  $R - R_{\odot}$  surface is  
followed down to new estimates for the reference values  
of  $X$  and  $\alpha_{ML}$ . This process is repeated until the dif-  
ference between successive  $X$  and  $\alpha_{ML}$  drops below one  
part in  $10^5$ .

Solar calibrated stellar models evolved using GS98  
OPAL and OPLIB opacity tables (Figure 5) differ  $\sim$   
0.5% in the SCSM hydrogen mass fractions and  $\sim 1.5\%$   
in the SCSM convective mixing length parameters (Ta-  
ble 1). While the two evolutionary tracks are very simi-  
lar, note that the OPLIB SCSM's luminosity is system-  
atically lower at the same effective temperature all the  
way from the premain sequence up and until the star  
leaves the main sequence, at which point it is effectively  
the same as the OPAL SCSM. This luminosity difference  
between OPAL and OPLIB based models is consistent  
with expectations given the steeper temperature gradi-  
ent the lower OPLIB opacities will result in.

#### 5. MODELING

In order to model the Jao Gap we evolve two extremely finely sampled mass grid of models. One of these grids uses the OPAL high-temperature opacity tables while the other uses the OPLIB tables. Each grid evolves a model every  $0.00025 M_{\odot}$  from  $0.2$  to  $0.4 M_{\odot}$  and every  $0.005 M_{\odot}$  from  $0.4$  to  $0.8 M_{\odot}$ . All models in both grids use a GS98 solar composition, the (1, 101, 0) **Free\_EOS** (version 2.7) configuration, and 1000 year old pre-main sequence polytropic models as their initial conditions.

Because in this work we are just interested in the location shift of the gap as the opacity source varies, we do not model variations in composition. **Others have done this and they have found blah....**

The variability leading to the gap is quite clear in the mass luminosity relation (Figures 6 & 7 **Make this figure for the two large runs**)

### 5.1. Population Synthetis

In order to compare the gap to observations we use in house population synthetis code. Our population synthetis code first uses inverse CDF sampling to build a distribution of target masses from some initial mass function (IMF). Specifically we use the **Sollima** IMF where, for masses  $0.25 M_{\odot} \leq M \leq 1 M_{\odot}$ ,  $\alpha = -1.34 \pm 0.07$ . The model nearest in mass to the samples mass above and the nearest model below are then selected from the evolved database. The surface gravity, luminosity, and effective temperature of the sample are then estimated through computing a linear interpolation between the bounding models and evaluating that interpolation at the sample mass.  $T_{eff}$ ,  $g$ , and  $\log(L)$  are transformed into Gaia G, BP, and RP magnitudes using the bolometric corrections provided by the Gaia Colaboration, specifically **feh000.UBVRiplus** [CITATION] [How to cite Aarons code]. Next, we introduce observationally informed photometric and astrometric Uncertainties into our population.

We select the Gaia Catalogue of Nearby Stars (GCNS) [CITATION] to empirically calibrate uncertainty relations. A function with the form of Equation 5 is fit to parallax uncertainty vs. G magnitude. Additionally, a function of the form of Equation 6 is fit to  $i^{\text{th}}$  (G, BP, RP) magnitude uncertainty vs.  $i^{\text{th}}$  magnitude.

$$\sigma_{plx}(M_g) = ae^{bM_g} + c \quad (5)$$

$$\sigma_i(M_i) = ae^{M_i - b} + c \quad (6)$$

Each of these functions then gives the an estimated uncertainty of some quantity at a given magnitude. For each sampled star in the synthetic population we sample

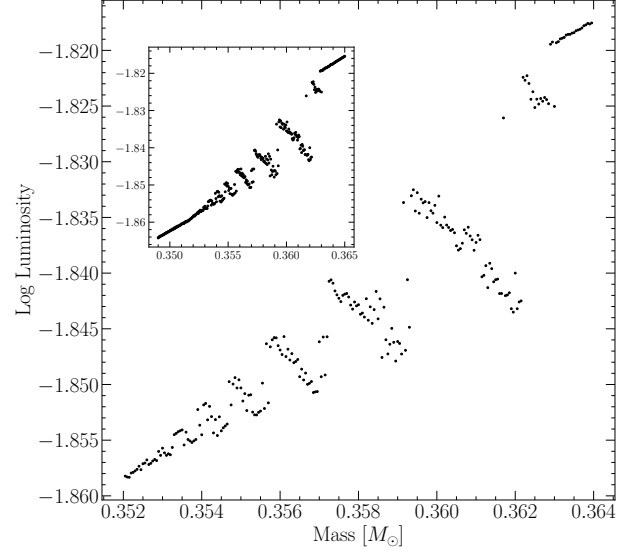


**Figure 6. THIS IS A TEST FIGURE, REPLACE WHEN LARGE RUN IS DONE**

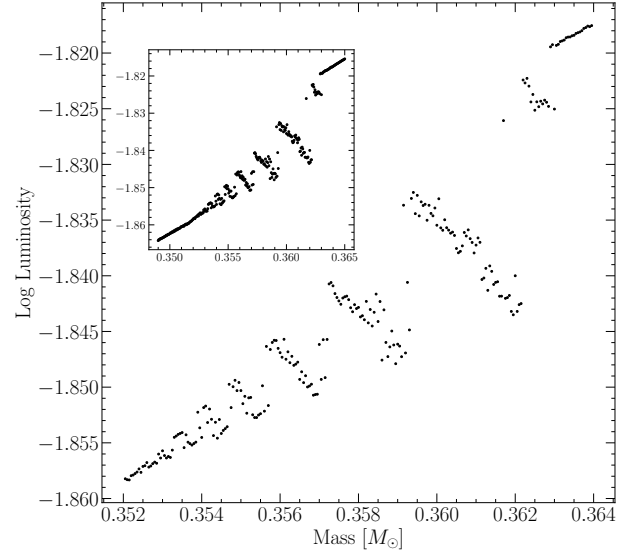


**Figure 7. THIS IS A TEST FIGURE, REPLACE WHEN LARGE RUN IS DONE**

a parallax from the parallax distribution of the GCNS (Figure 8), referred to as the "true parallax". A parallax uncertainty is calculated based on the G magnitude of the synthetic star (hereafter the "true G magnitude") and the results of the fitting described in the previous paragraph. This uncertainty then will, with equal weighting, either be added or subtracted from the true parallax, yeilding an "observed parallax". The true parallax will be used to convert the true  $i^{\text{th}}$  magnitude to an apparent  $i^{\text{th}}$  magnitude and the observed parallax will be used to convert the apparent  $i^{\text{th}}$  magnitude into an observed  $i^{\text{th}}$  magnitude. Finally, each observed magnitude is summed with an estimated uncertainty for

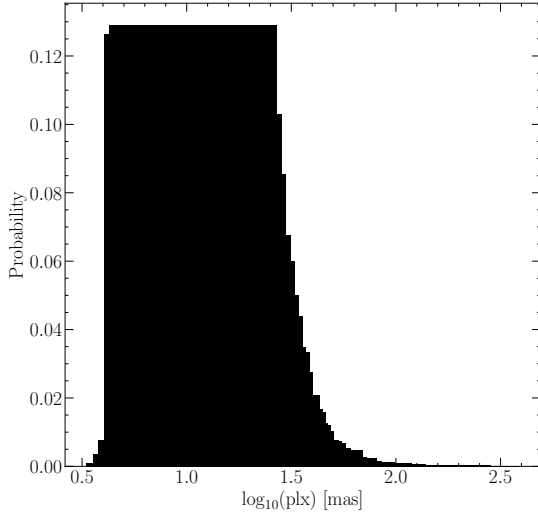


**Figure 8.** Probability distribution sampled when assigning true parallaxes to synthetic stars. This distribution is built from the GCNS.

that magnitude based on the fit of the  $i^{\text{th}}$  magnitude to the uncertainty in the  $i^{\text{th}}$  magnitude.

To summarize the process that each synthetic star will go through

1. Sample from a Sollima (2019) IMF to determine synthetic star mass
2. Find the closest model above and below the synthetic star, linearly interpolate model parameters to the synthetic star mass.
3. Convert synthetic star  $g$ ,  $T_{\text{eff}}$ , and  $\text{Log}(L)$  to Gaia G, BP, and RP colors.
4. Sample from the GCNS to assign synthetic star a “true” parallax.
5. Evaluate the empirical calibration given in Equation 5 to find an associated parallax uncertainty and adjust the true parallax by this value resulting in an observed parallax.
6. Use the true parallax to find an apparent magnitude for each filter.
7. Use the observed parallax and the apparent magnitude to find an observed magnitude
8. Evaluate the empirical calibration given in Equation 6 to give a magnitude uncertainty scale in each band.

Model	Location	Prominence
OPAL	10.15864	0.19501
OPLIB 1	10.17813	0.26055
OPLIB 2	10.21313	0.46898

**Table 2.** Locations identified as potential gaps.

9. Adjust each magnitude by some amount sampled from a normal distribution with a standard deviation of the magnitude uncertainty scale.

This method then incorporates both photometric and astrometric Uncertainties into our population synthesis. Seven Gyr old synthetic populations using OPAL and OPLIB opacities are given in Figure 9.

## 6. RESULTS

We quantify the Jao Gap location along the magnitude axis by first subsampling our synthetic populations, finding the linear number density along the magnitude axis of each subsample, averaging these linear number density and extracting peaks from this above a prominence threshold. Once we have the peak location we fit a gaussian to a window centered at the peak giving both an estimate of the gap location and the gap width. Figure 10 shows this fit for both OPAL and OPLIB populations.

Our gap identification method finds two potential gaps in the OPLIB (Table 2) data while only finding one in the OPAL dataset. This apparent discrepancy is not due to a fundamental structural difference between the OPAL and OPLIB opacity tables; rather, it is attributable to the phasing of the periodic luminosity variations seen across mass in Figures 6 and 7 and whether or not the injected noise smears all of these together into one gap or two gaps. [Run a test where you manually shift the OPAL data to the same phase as the OPLIB data to show that this has the effect of making two gaps show up].

Both gaps identified in the OPLIB sample are at fainter magnitudes than the gap identified in the OPAL sample. This implies that in the OPLIB sample the convective mixing events which drive the kissing instability should happen more regularly and therefore also start earlier in the models evolution. This is because each mixing event serves to interrupt the “standard” luminosity evolution of a stellar model, kicking its luminosity back down to what it would have been a few Gyrs earlier instead of allowing it to slowly increase. Looking at the interior physics of one OPAL and one OPLIB model shows that this shorter duration between mixing events is in fact seen (Figure [PUT KIPPENHAN DIAGRM HERE]).

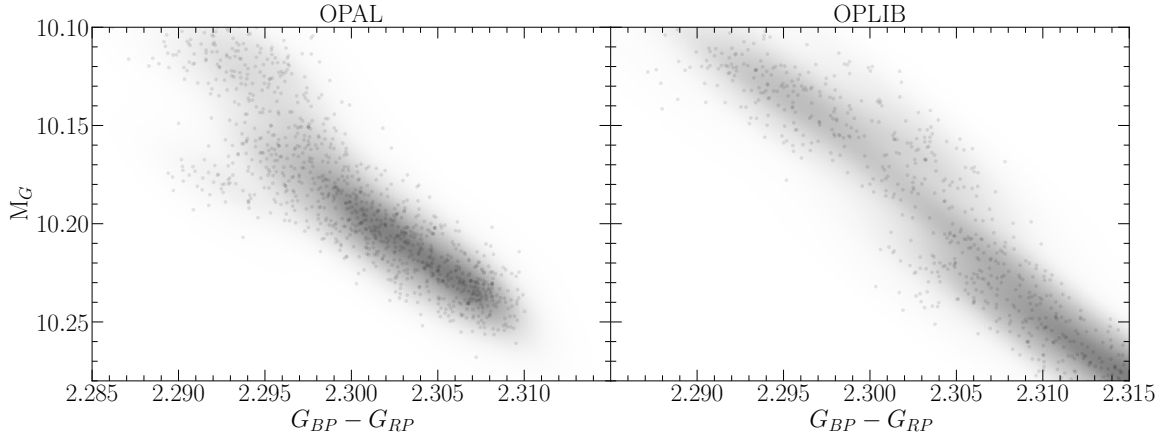


**Figure 9.** Population synthesis result for models evolved with OPAL (left) and models evolved with OPLIB (right). A gaussian kernel-density-estimate has been overlayed to better highlight the density variations. [THIS IS A PLACEHOLDER FIGURE]

The slightly lower opacities characteristic to OPLIB serve to shallow the radiative temperature gradient,  $\nabla T_{rad}$ ; however, as the adiabatic temperature gradient remains essentially unchanged, a larger interior radius of the model will remain unstable to convection [CHECK IF THIS OR IF RADIATIVE ZONE MOVING IN]. This larger convective zone and therefore smaller radiative zone is in line with the behavior of the models presented here. We see that OPLIB models undergo convective mixing events earlier in their evolution than OPAL models (Figure 11 implying that the inner convective zone did not have to expand as much to meet the outer convective zone.

Then compare the results to observations, comment on which one matches observations better and also how confident we can be about that

Comment on if the shift in the gap location is larger or smaller than the size of the gap or the shift due to other effects such as variations in age or composition, i.e. is it significant enough to matter

comment on why the gap shifts in the manner which it does, i.e. the opacities are lower. Show how for a constant opacity table increasing the metallicity (which will also change the opacity) affects the gap location

## 7. CONCLUSION

## REFERENCES

- Amard, L., Palacios, A., Charbonnel, C., et al. 2019, *A&A*, 631, A77, doi: [10.1051/0004-6361/201935160](https://doi.org/10.1051/0004-6361/201935160)
- Baraffe, I., & Chabrier, G. 2018, *A&A*, 619, A177, doi: [10.1051/0004-6361/201834062](https://doi.org/10.1051/0004-6361/201834062)
- Chabrier, G., & Baraffe, I. 1997, *A&A*, 327, 1039. <https://arxiv.org/abs/astro-ph/9704118>
- Chandra, R. V., & Varanasi, B. S. 2015, *Python requests essentials* (Packt Publishing Ltd)
- Choi, J., Dotter, A., Conroy, C., et al. 2016, *ApJ*, 823, 102, doi: [10.3847/0004-637X/823/2/102](https://doi.org/10.3847/0004-637X/823/2/102)
- Colgan, J., Kilcrease, D. P., Magee, N. H., et al. 2016, in *APS Meeting Abstracts*, Vol. 2016, APS Division of Atomic, Molecular and Optical Physics Meeting Abstracts, D1.008
- DIERCKX, P. 1981, *IMA Journal of Numerical Analysis*, 1, 267, doi: [10.1093/imanum/1.3.267](https://doi.org/10.1093/imanum/1.3.267)
- Dotter, A., Chaboyer, B., Jevremović, D., et al. 2008, *The Astrophysical Journal Supplement Series*, 178, 89
- Feiden, G. A., Skidmore, K., & Jao, W.-C. 2021, *ApJ*, 907, 53, doi: [10.3847/1538-4357/abcc03](https://doi.org/10.3847/1538-4357/abcc03)
- Fontes, C. J., Zhang, H. L., Abdallah, J., J., et al. 2015, *Journal of Physics B Atomic Molecular Physics*, 48, 144014, doi: [10.1088/0953-4075/48/14/144014](https://doi.org/10.1088/0953-4075/48/14/144014)
- Iglesias, C. A., & Rogers, F. J. 1996, *ApJ*, 464, 943, doi: [10.1086/177381](https://doi.org/10.1086/177381)
- Jao, W.-C., & Feiden, G. A. 2020, *AJ*, 160, 102, doi: [10.3847/1538-3881/aba192](https://doi.org/10.3847/1538-3881/aba192)
- Jao, W.-C., Henry, T. J., Gies, D. R., & Hambly, N. C. 2018, *ApJL*, 861, L11, doi: [10.3847/2041-8213/aacdf6](https://doi.org/10.3847/2041-8213/aacdf6)
- Magee, N. H., Abdallah, J., Colgan, J., et al. 2004, in *American Institute of Physics Conference Series*, Vol. 730, *Atomic Processes in Plasmas: 14th APS Topical Conference on Atomic Processes in Plasmas*, ed. J. S. Cohen, D. P. Kilcrease, & S. Mazavet, 168–179
- Mansfield, S., & Kroupa, P. 2021, *A&A*, 650, A184, doi: [10.1051/0004-6361/202140536](https://doi.org/10.1051/0004-6361/202140536)



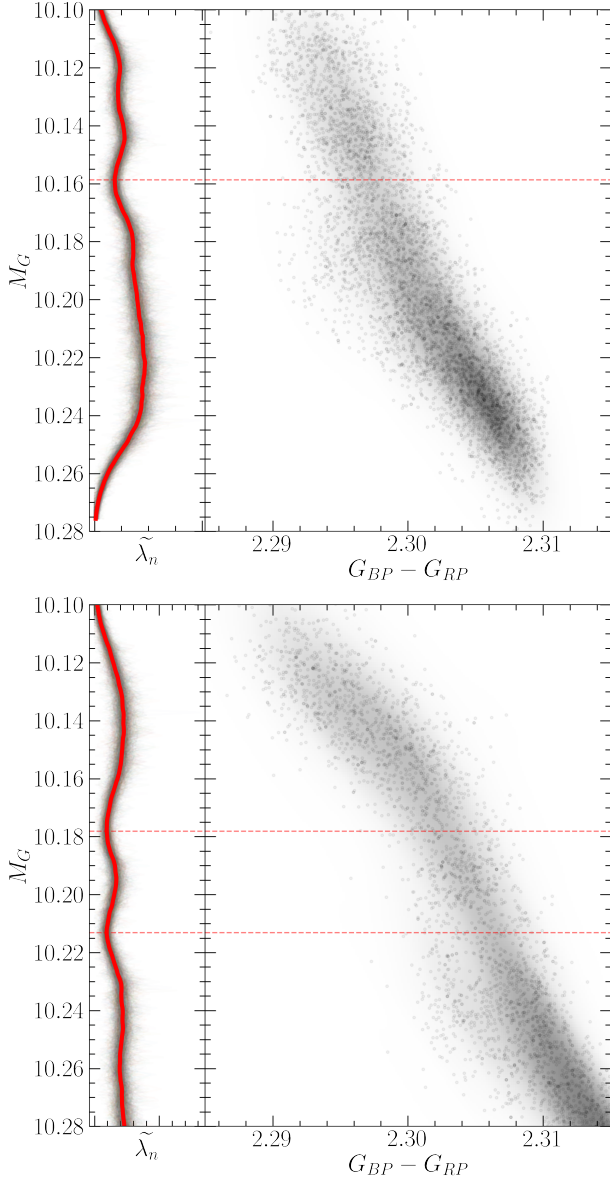


**Figure 10.** (right panels) OPAL (top) and OPLIB (bottom) synthetic populations. (left panels) Normalized linear number density along the magnitude axis. A dashed line has been extended from the peak through both panels to make clear where the Identified Jao Gap location is wrt. to the population.

- 523 Nutzman, P., & Charbonneau, D. 2008, *PASP*, 120, 317,  
 524 doi: [10.1086/533420](https://doi.org/10.1086/533420)  
 525 Richardson, L. 2007, *April*  
 526 Rodríguez-López, C. 2019, *Frontiers in Astronomy and*  
 527 *Space Sciences*, 6, 76, doi: [10.3389/fspas.2019.00076](https://doi.org/10.3389/fspas.2019.00076)  
 528 Seaton, M. J., Yan, Y., Mihalas, D., & Pradhan, A. K.  
 529 1994, *MNRAS*, 266, 805, doi: [10.1093/mnras/266.4.805](https://doi.org/10.1093/mnras/266.4.805)

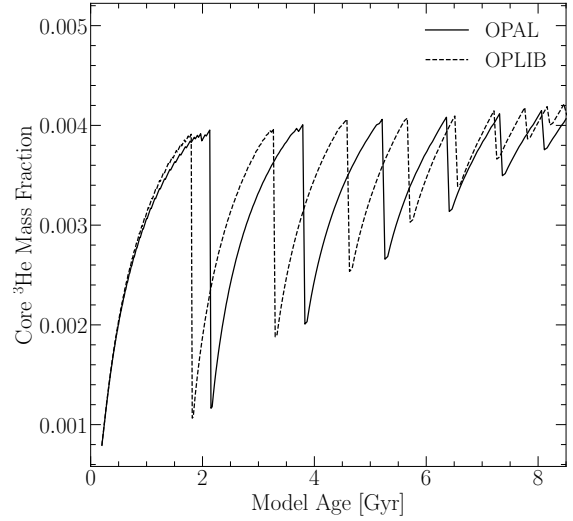


**Figure 11.** Core  ${}^3\text{He}$  mass fraction for a model evolved with OPAL and a model evolved with OPLIB within the Jao Gap's mass range. Note how the OPLIB model undergoes the mixing event earlier in its evolution than the OPAL model does.

- 530 Sollima, A. 2019, *Monthly Notices of the Royal*  
 531 *Astronomical Society*, 489, 2377,  
 532 doi: [10.1093/mnras/stz2093](https://doi.org/10.1093/mnras/stz2093)  
 533 van Saders, J. L., & Pinsonneault, M. H. 2012, *ApJ*, 751,  
 534 98, doi: [10.1088/0004-637X/751/2/98](https://doi.org/10.1088/0004-637X/751/2/98)  
 535 Virtanen, P., Gommers, R., Oliphant, T. E., et al. 2020,  
 536 *Nature Methods*, 17, 261, doi: [10.1038/s41592-019-0686-2](https://doi.org/10.1038/s41592-019-0686-2)